

# Network-Based Characterization of Blood Large-Scale Coherent Motion in the Healthy Human Aorta With 4D Flow MRI

Karol Calò <sup>1</sup>, Diego Gallo <sup>1</sup>, Andrea Guala <sup>1</sup>, Maurizio Lodi Rizzini, Lydia Dux-Santoy <sup>1</sup>, Jose Rodriguez-Palomares <sup>1</sup>, Stefania Scarsoglio <sup>1</sup>, Luca Ridolfi <sup>1</sup>, and Umberto Morbiducci <sup>1</sup>

**Abstract—Objective:** The need for distilling the hemodynamic complexity of aortic flows into clinically relevant quantities resulted in a loss of the information hidden in 4D aortic fluid structures. To reduce information loss, this study proposes a network-based approach to identify and characterize in vivo the large-scale coherent motion of blood in the healthy human aorta. **Methods:** The quantitative paradigm of the aortic flow as a “social network” was applied on 4D flow MRI acquisitions performed on forty-one healthy volunteers. Correlations between the aortic blood flow rate waveform at the proximal ascending aorta (AAo), assumed as one of the drivers of aortic hemodynamics, and the waveforms of the axial velocity in the whole aorta were used to build “one-to-all” networks. The impact of the driving flow rate waveform and of aortic geometric attributes on the transport of large-scale coherent fluid structures was investigated. **Results:** The anatomical length of persistence of large-scale coherent motion was the 29.6% of the healthy thoracic aorta length (median value, IQR 23.1%–33.9%). Such length is significantly influenced by the average and peak-to-peak AAo blood flow rate values, suggesting a remarkable inertial effect of the AAo flow rate on the transport of large-scale fluid structures in the distal aorta. Aortic geometric attributes such as curvature, torsion and arch shape did not influence the anatomical length of persistence. **Conclusion:** The proposed in vivo approach allowed to quantitatively characterize the transport of large-scale fluid structures in the healthy aorta, strengthening the definition of coherent hemodynamic structures and identifying flow inertia rather than geometry as one of its main determinants. **Significance:** The findings on healthy aortas may

be used as reference values to investigate the impact of aortic disease or implanted devices in disrupting/restoring the physiological spatiotemporal coherence of large-scale aortic flow.

**Index Terms—**Aorta, coherent flow structures, complex networks, hemodynamics, spatiotemporal analysis.

## I. INTRODUCTION

THE human aorta represents a site where theoretical and applied fluid mechanics have been challenged to interpret the physiological and pathological significance of specific hemodynamic profiles. The spatiotemporal heterogeneity of aortic flow patterns in healthy subjects is the consequence of the interaction of (1) the natural asymmetry of the vascular anatomy, exacerbated by the non-planar curvature of the ascending (AAo), transverse and descending aortas (DAo) [1], [2], (2) the aortic wall motion and distensibility, (3) the complex flow structures developing into the streaming blood as a consequence of aortic valve opening/closure [3], and (4) the momentum imparted to blood flow by the ventricular twisting and torsion during contraction [4], [5]. All those factors lead to the production and transport of large-scale fluid structures characterized by a non-trivial composition of antegrade and retrograde axial flows with secondary flows (the helical flow patterns) [5], [6], [7], [8], [9], [10], [11], [12], [13], [14]. The endeavor of deciphering the physiological significance of aortic hemodynamics is complicated by the marked intersubject variability characterizing the healthy human aorta [7], so that distinct aortic hemodynamic profiles may not unambiguously emerge. Moreover, the complex, unsteady dynamics of the aortic flow challenges the definition, extraction, and understanding of fundamental, coherent flow structures characterizing the hemodynamics of the healthy aorta. This incomplete characterization thereby hampers: (1) the clear comprehension of those flow-mediated mechanisms leading to the pathogenesis of aortic diseases [15], [16], [17], [18]; (2) the identification of effective, non-invasively measurable hemodynamic markers of risk of onset/progression of aortic disease [18], [19].

These considerations hold true despite the possibility of non-invasively measuring the large-scale structures of the aortic hemodynamics with advanced flow imaging approaches. In particular, the use of 4D flow MRI has grown in the last decades,

Manuscript received 26 April 2022; revised 25 July 2022; accepted 21 September 2022. Date of publication 26 September 2022; date of current version 20 February 2023. The work of Andrea Guala was supported by the Spanish Ministry of Science, Innovation and Universities under Grant IJC2018-037349-I. The work of Karol Calò, Diego Gallo, Maurizio Lodi Rizzini, and Umberto Morbiducci was supported by MIUR FISR—FISR2019\_03221 CECOMES. (Corresponding author: Umberto Morbiducci.)

Karol Calò, Diego Gallo, Maurizio Lodi Rizzini, and Stefania Scarsoglio are with the PoliToBIOMed Lab, Department of Mechanical and Aerospace Engineering, Politecnico di Torino, Italy.

Andrea Guala, Lydia Dux-Santoy, and Jose Rodriguez-Palomares are with the Vall d’Hebron Institut de Recerca, Spain, and also with the CIBER-CV, Instituto de Salud Carlos III, Spain.

Luca Ridolfi is with the PoliToBIOMed Lab, Department of Environment, Land and Infrastructure Engineering, Politecnico di Torino, Italy.

Umberto Morbiducci is with the PoliToBIOMed Lab, Department of Mechanical and Aerospace Engineering, Politecnico di Torino, 10129 Turin, Italy (e-mail: umberto.morbiducci@polito.it).

Digital Object Identifier 10.1109/TBME.2022.3209736

becoming the gold standard in vivo technology for aortic flow visualization and characterization [8], [13], [15], [19], [20], [21], [22], [23], [24], [25], even if still affected by moderate spatial and temporal resolution.

The present study is motivated by the need of identifying and interpreting coherent large-scale flow structures [26] as those structures dictating the organization of aortic hemodynamics. To do that, building on very recent applications of the Complex Networks (CNs) theory [27] to characterize cardiovascular flows as “social networks” in silico [28], [29], [30] and in vivo [13], a network-based approach is proposed to analyze in vivo the spatiotemporal correlation of large-scale flow structures in a 4D flow MRI dataset of healthy thoracic aortas [22]. In detail, aortic flow similarity is quantified in terms of correlation coefficient between the axial component of time-resolved velocity waveforms measured in each voxel of the aortic domain (i.e., the local blood velocity vector component aligned with the main flow direction as identified by the local tangent vector to the aortic main axis [31]) and the flow rate waveform measured in the AAO, the latter being considered as one of the main “driving terms” of the large-scale dominant aortic flow patterns. The correlation-based analysis is used to build subject-specific “one-to-all” networks, consisting of one reference node at the sinotubular junction (STJ) connected to all the voxels (nodes) in the aortic domain. This connection is weighted by the correlation between the axial component of the velocity waveform measured in that voxel and the AAO blood flow rate waveform at the STJ. Through the definition of *ad-hoc* network metrics, it is possible to rigorously determine the anatomical length of persistence of these correlations and explore its relationships with blood flow rate waveform dynamics as well as with main geometric attributes of the aorta.

The findings of this study highlight the potential of the “one-to-all” network approach in investigating the impact that aortic blood flow rate waveform’s shapes/attributes have on the spatiotemporal coherence of large-scale fluid structures, uncovering features characterizing the hemodynamics of the healthy human aorta with in vivo measurement.

## II. METHODS

### A. Study Population

Forty-one healthy volunteers presenting with a tricuspid aortic valve (TAV) were enrolled for this study (15 females, age:  $38.21 \pm 12.04$  years, BSA:  $1.83 \pm 0.15$  m<sup>2</sup>, ascending aorta diameter:  $28.15 \pm 3.78$  mm, heart rate:  $61.08 \pm 11.50$  bpm). The study was approved by the ethical committee of the Vall d’Hebron Hospital (protocol n°:ID-RTF079, December 28th, 2016) and informed consent was obtained from all participants. [22].

### B. 4D Flow MRI Acquisition Protocol and Data Analysis

An overview of the methods applied in this study is provided in Fig. 1. 4D flow MRI acquisitions of the entire thoracic aorta were obtained using a 1.5 T Signa scanner (GE Healthcare, Waukesha, WI, USA), with retrospective ECG gating during free-breathing with no endovenous contrast agent administration. A radially

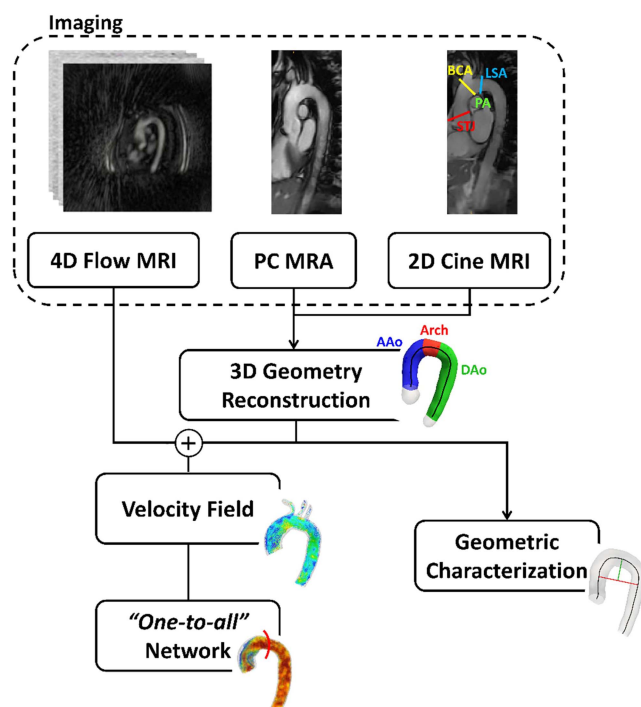


Fig. 1. Schematic diagram of the study design, showing how imaging data contribute to define vessel geometry, “one-to-all” network analysis, and geometric characterization. PC MRA: phase-contrast MR angiography; STJ: sinotubular junction; BCA: brachiocephalic artery; LSA: left subclavian artery; PA: pulmonary artery; AAO: ascending aorta; DAO: descending aorta.

undersampled acquisition with five-point balanced velocity encoding [32] was set according to the following scheme: velocity encoding of 200 cm/s, field of view  $400 \text{ mm} \times 400 \text{ mm} \times 400 \text{ mm}$ , scan matrix  $160 \times 160 \times 160$ , voxel size  $2.5 \text{ mm} \times 2.5 \text{ mm} \times 2.5 \text{ mm}$ , time resolution and number of cardiac frames in the range of 22.3–41.6 ms and 25–54, respectively. The 4D flow MRI studies were reconstructed offline according to the nominal temporal resolution ( $5 \times \text{TR}$ ) of each patient as described elsewhere [13], [22], [32]. The adopted 4D flow MRI acquisition protocol has been exhaustively reported elsewhere [13], [22], [32]. The segmentation of the whole thoracic aorta was performed using a semi-automatic approach from phase-contrast MR angiography (PC MRA) using ITK-Snap [13]. The three-dimensional model of the aorta was reconstructed from the segmented images and the aortic centerline was extracted using VMTK ([www.vmtk.org](http://www.vmtk.org)) (Fig. 1). The sinotubular junction (STJ), the brachiocephalic artery (BCA), the left subclavian artery (LSA), and the pulmonary artery (PA) bifurcation were identified adopting co-registered 2D cine images (Fig. 1) and used as anatomical landmarks to ensure a consistent spatial extent across all individual aortas [13]. Based on landmarks, the aorta was divided into three regions: the ascending aorta (AAo), the aortic arch, and the descending aorta (DAo). The DAo was delimited distally by a cross-section located 12 maximally inscribed spheres radii downstream of the LSA bifurcation. The three-dimensional segmentation of the aorta was used to mask the acquired velocity data.

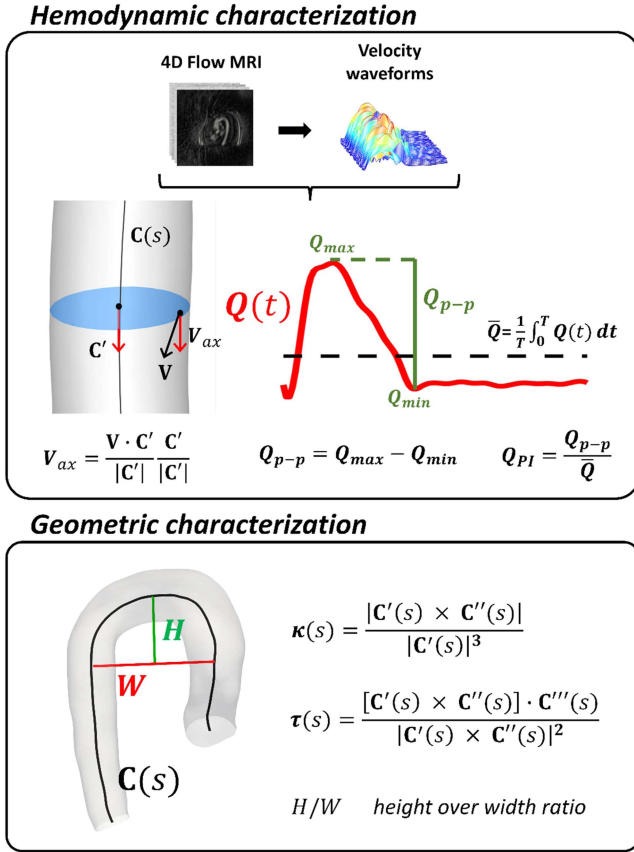


Fig. 2. Methodology for the hemodynamic and geometric characterization of the investigated aortas. Hemodynamic characterization panel:  $\mathbf{V}$ : blood velocity vector;  $\mathbf{C}(s)$ : vessel centerline, as a function of the curvilinear abscissa  $s$ ;  $\mathbf{C}'$ : vector tangent to the centerline;  $T$ : period of the cardiac cycle;  $Q_{max}$ : blood flow rate maximum value at the systolic phase;  $Q_{min}$ : blood flow rate minimum value soon after the systolic phase. Geometric characterization panel:  $\mathbf{C}'(s)$ ,  $\mathbf{C}''(s)$ ,  $\mathbf{C}'''(s)$ : 1<sup>st</sup>, 2<sup>nd</sup>, and 3<sup>rd</sup> derivatives of  $\mathbf{C}(s)$ .

### C. Aortic Hemodynamic and Geometric Characterization

The acquired three phase-contrast (velocity) time-resolved waveforms (along the reconstructed cardiac cycle) were extracted from each aortic voxel [22] and the 4D velocity data were exported using in-house Matlab code (MathWorks Inc, USA). On each voxel, the waveform of the axial (through-plane) velocity component  $V_{ax}(t)$  along the cardiac cycle was derived and used to characterize the large-scale dominant aortic flow features. In detail,  $V_{ax}$  was calculated by projecting the local velocity vector  $\mathbf{V}$  along the direction of the tangent vector to the local vessel centerline (i.e., the local axial direction, Fig. 2) [13], [31]. Positive values of  $V_{ax}$  are representative of antegrade flow -along the main (i.e., proximal-to-distal) flow direction-, whereas negative values indicate retrograde flow [13], [31]. On each aorta, the acquired 3D velocity data were also used to reconstruct the blood flow rate waveform along the cardiac cycle  $Q(t)$  at the STJ (Fig. 2). The subject-specific  $Q(t)$  waveform was characterized in terms of cycle-averaged value  $\bar{Q}$ , peak-to-peak amplitude  $Q_{p-p}$ , and pulsatility index  $Q_{PI}$ , as in Fig. 2.

Given the impact of the non-planar asymmetry and curvature of the AAO and aortic arch on intravascular flow [1], [33] a

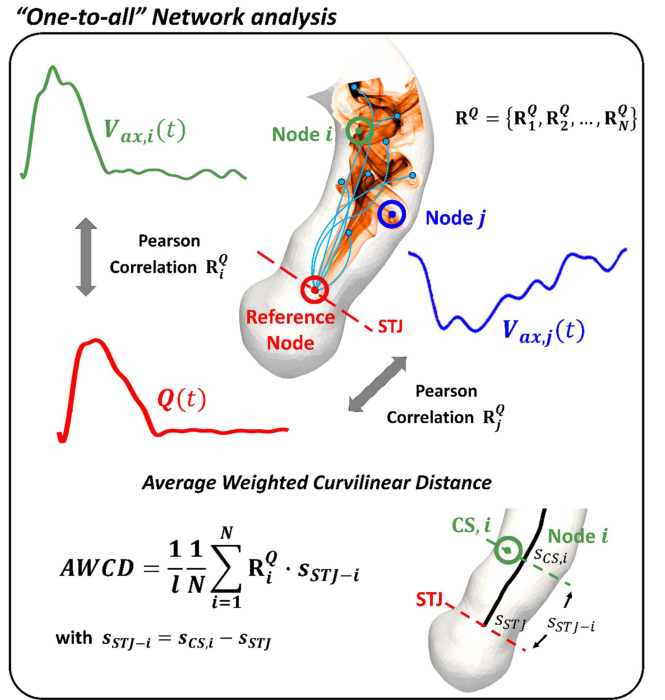


Fig. 3. Methodology for the "one-to-all" network analysis.  $CS, i$ : cross-section containing node  $i$ ;  $s_{CS,i}$ : curvilinear abscissa defining the cross-section  $CS, i$ ;  $s_{STJ}$ : curvilinear abscissa defining the STJ cross-section;  $s_{STJ-i}$ : curvilinear distance between node  $i$  and the reference node at STJ.

geometric analysis was performed adopting a centerline-based approach (Fig. 2). In particular, the aortic geometry was characterized in terms of: average curvature  $\bar{\kappa}$  and torsion  $\bar{\tau}$  [13], [34]; width  $W$  of the aortic arch (the distance between the centerline points of the AAO and DAAo at the level of the right PA); height  $H$  of the aortic arch (the maximal vertical distance between  $W$  and the highest point of the aortic arch); height over width ratio  $H/W$  [35].

Finally, pulse wave velocity (PWV), a descriptor of aortic stiffness, was non-invasively quantified from in vivo 4D flow MRI data using a wavelet-based method proposed in previous studies [36], [37].

### D. "One-to-All" Networks Construction and Characterization

Following a recent in silico study on carotid bifurcation hemodynamics [28], here a "one-to-all" network approach was adopted to explore in vivo the nature of the relationship between blood flow rate in the AAO and large-scale fluid structures. As sketched in Fig. 3, the "one-to-all" network built up within each aorta is made of: (1) one reference node located at the center of mass of the STJ section, characterized by the blood flow rate waveform  $Q(t)$ ; (2) all the  $N$  voxels of the investigated aortic domain located downstream of the STJ, each one characterized by the axial velocity waveform  $V_{ax,i}(t)$  (for  $i = 1, \dots, N$ ). For each acquired aorta the vector  $\mathbf{R}^Q = \{\mathbf{R}_1^Q, \mathbf{R}_2^Q, \dots, \mathbf{R}_N^Q\}$  of the Pearson correlation coefficients calculated between  $Q(t)$  and the  $V_{ax}(t)$  waveform at each of the  $N$  voxels was obtained (Fig. 3).

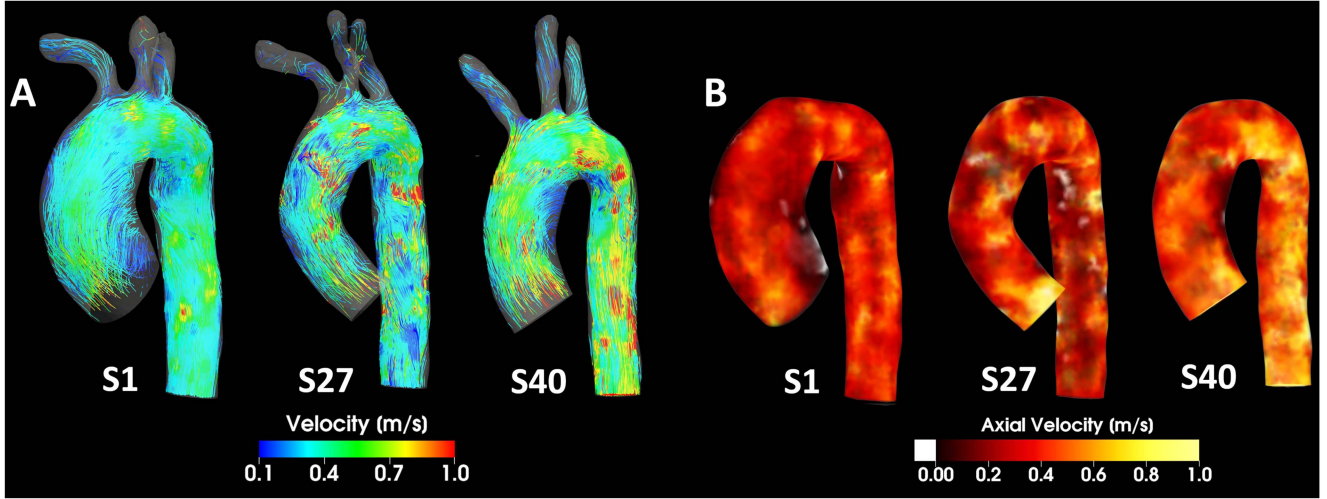


Fig. 4. Visualizations of: (A) instantaneous streamlines colored by the velocity magnitude value, and (B) volumetric maps of instantaneous axial velocity  $V_{ax}$  (white color represents negative  $V_{ax}$  values, i.e., retrograde flow) at the maximum deceleration phase, in three representative subjects. Reconstructed geometries are shown with different scales.

The  $R_i^Q$  value, which measures the dynamic similarity between the driving waveform  $Q(t)$  and the axial velocity waveform measured in the  $i$ -th voxel, was then used to weight the link between the reference node and the generic node  $i$  of the network.

To quantify the anatomical length of persistence of the  $Q(t)$ - $V_{ax}(t)$  waveforms correlation, a network metric, the *Average Weighted Curvilinear Distance* (*AWCD*), was here defined as:

$$AWCD = \frac{1}{l} \frac{1}{N} \sum_{i=1}^N R_i^Q \cdot s_{STJ-i}, \quad (1)$$

where  $l$  is the length of the centerline of the thoracic aorta,  $N$  is the number of voxels (nodes) in the aortic fluid domain,  $s_{STJ-i}$  is the curvilinear distance between the reference node at STJ and the  $i$ -th voxel (intended as the difference between the curvilinear abscissa values defining the cross-section containing node  $i$ , and the STJ cross-section, Fig. 3), respectively. The *AWCD* measures the average curvilinear distance from the reference point, weighted by the correlation coefficient  $R_i^Q$ , thus providing the anatomical distance from the STJ over which the similarity of the local axial velocity waveforms with the driving waveform  $Q(t)$  propagates inside the aortic fluid domain. To account for the inter-individual geometric variability of healthy human aorta [7], the *AWCD* was normalized with respect to the thoracic aorta centerline length  $l$  comprised between the STJ cross-section and the distal DAo cross-section. According to (1), by construction two voxels (nodes)  $i$  and  $j$  with  $R_i^Q = R_j^Q$  and  $s_{STJ-i} > s_{STJ-j}$  contribute differently to *AWCD*, as the voxel (node)  $i$  located more distal contributes more than voxel (node)  $j$ .

The Spearman correlation was adopted to explore the existence of associations of *AWCD* with blood flow rate dynamics at STJ and with aortic geometry attributes. Kruskal-Wallis and Mann-Whitney U statistical tests were used to assess if the distributions of the investigated quantities belong to the same population. Statistical significance was assumed for  $p < 0.05$ .

TABLE I  
ANATOMICAL AND HEMODYNAMIC DESCRIPTORS

Quantity	
$\bar{\kappa}$ , mm <sup>-1</sup>	0.024 (0.022-0.025)
$\bar{\tau}$ , mm <sup>-1</sup>	0.098 (0.081-0.125)
$H$ , mm	27.829 (24.065-32.854)
$W$ , mm	64.424 (57.193-70.700)
$H/W$	0.432 (0.379-0.516)
$\bar{Q}$ , l min <sup>-1</sup>	2.957 (2.529-3.524)
$Q_{p-p}$ , l min <sup>-1</sup>	15.525 (12.656-20.465)
$Q_{PI}$	5.105 (4.517-6.099)
PWV, m s <sup>-1</sup>	5.240 (4.190-6.250)
<i>AWCD</i>	0.296 (0.231-0.339)

Anatomical and hemodynamic descriptors are expressed as median (interquartile range, IQR) of the cumulative distribution.

### III. RESULTS

#### A. Anatomical and Hemodynamic Quantities

The distributions (in terms of median value and interquartile range IQR) of anatomical and hemodynamic quantities characterizing the dataset of 41 healthy human aortas are reported in Table I.

#### B. Large-Scale Aortic Hemodynamics

An overview of the large-scale aortic hemodynamic patterns in the investigated subjects is provided in Fig. 4. The instantaneous streamlines at the maximum deceleration phase of the cardiac cycle are displayed for three representative cases, characterized by a low, average, and high  $H/W$  value, respectively (subjects S1, S27 and S40 in Fig. 4(A)). In general, and as expected, low-velocity flow separation and recirculation regions are observed at the inner wall of the AAO and of the proximal DAo.

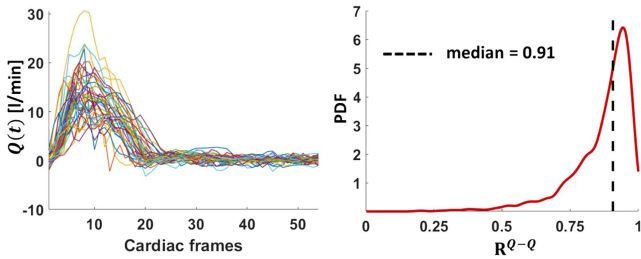


Fig. 5. Subject-specific blood flow rate waveforms  $Q(t)$  at STJ of the investigated healthy aortas (left panel). Probability density function (PDF) of the correlation coefficients  $R^{Q-Q}$  between all pairs of  $Q(t)$  waveforms (right panel).

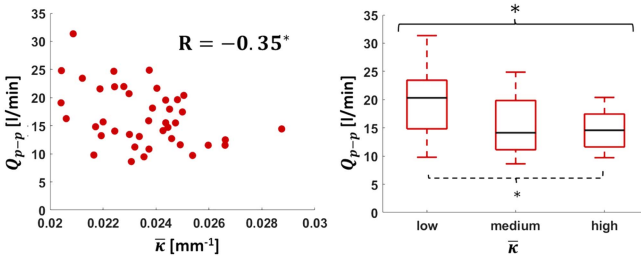


Fig. 6. Scatter plot of blood flow rate peak-to-peak amplitude  $Q_{p-p}$  vs. aortic mean curvature  $\bar{\kappa}$  (left panel). Box plots comparing  $Q_{p-p}$  distributions obtained by dividing  $\bar{\kappa}$  in three groups based on tertile values (right panel).  $R$ : Spearman correlation coefficient. Statistical significance is indicated with: \* $p < 0.05$ ; † $p < 0.01$ ; ‡ $p < 0.001$ .

The corresponding volumetric maps of  $V_{ax}$  (Fig. 4(B)) highlight that: high  $V_{ax}$  values are observed in the proximal AAO due to the aortic valve outflow jet; in subjects characterized by high  $H/W$  value high axial velocity flow patterns are present also in the DAO portion (see subject S40 in Fig. 4(B)); negative, low magnitude  $V_{ax}$  patterns develop at the AAO inner wall, where flow reversal occurs in correspondence of the separation region also highlighted using streamlines visualization (see subjects S1 and S40, Fig. 4).

### C. Analysis of Blood Flow Rate Waveforms at STJ

The blood flow rate waveforms at the STJ for all investigated cases are shown in Fig. 5. The expected, marked similarity of  $Q(t)$  waveforms measured at the STJ in healthy aortas is quantitatively confirmed by the distribution of the Pearson correlation coefficients  $R^{Q-Q}$  (Fig. 5) computed between each pair of  $Q(t)$  waveforms (median value  $\hat{R}^{Q-Q} = 0.907$ , IQR 0.820–0.946). The results presented in Fig. 5 suggest a low intersubject variability of  $Q(t)$  waveforms in physiological conditions.

From the exploration of the relationships between  $Q(t)$  waveforms and geometric attributes a moderate significant correlation emerged only between aortic curvature and  $Q(t)$  waveforms dynamics: the scatter plot in Fig. 6 highlights the existence of a negative association between the average curvature  $\bar{\kappa}$  and the peak-to-peak amplitude of blood flow rate waveform at STJ,  $Q_{p-p}$  ( $R = -0.35$ ,  $p = 0.02$ ). Moreover, significant differences in  $Q_{p-p}$  values emerged stratifying the 41 healthy aortas in three groups based on the tertile values of the distribution of

the average curvature  $\bar{\kappa}$  ( $p = 0.04$ , boxplots in Fig. 6), with significantly different  $Q_{p-p}$  values between groups presenting with low and high average curvature  $\bar{\kappa}$  ( $p = 0.02$ ). No association emerged between aortic blood flow rate features at STJ and PWV.

### D. “One-to-All” Network Analysis of Aortic Flow

The “one-to-all” network is designed to explore the organization level of large-scale aortic flow patterns. The analysis of the distribution of the correlation coefficients  $R^Q$  inside individual aortas highlights that in general axial velocity waveforms along the cardiac cycle are characterized by a remarkable dynamical similarity with the flow rate waveform at STJ, although with some intersubject variability (cumulative median value  $\hat{R}^Q = 0.69$ , cumulative IQR = 0.843–0.455, Fig. 7(A)). This emergent behavior is confirmed by the visualization of the individual aortic volumetric maps displaying  $R^Q$  values above the cumulative median  $\hat{R}^Q$  (Fig. 7(B)). It can be observed that: (1) in those subjects where  $V_{ax}(t)$  waveforms present high dynamic similarity with  $Q(t)$  waveform at STJ (e.g., subjects S1, S3, S6, S15, S30, S38–S41), the highest  $R^Q$  values (above 0.90) are mainly located in the AAO; (2) the similarity between blood flow rate and the axial velocity waveforms can be lost or markedly reduced within the aortic arch, but it can be restored distally within the DAO, according to the restoration of a predominant axial forward blood flow. Conversely, when  $R^Q$  values are well below the cumulative median  $\hat{R}^Q$ , the highest correlation values (above 0.85) are again located in the AAO and/or in the distal portion of the DAO (e.g., subjects S8, S10–S13, S23, S26, S33, and S34 in Fig. 7(B)). The portions of aorta in Fig. 7(B) characterized by a low degree of dynamical similarity with the blood flow rate at STJ include  $V_{ax}(t)$  waveforms with either low positive or negative  $R^Q$  values. As an example, the volumetric map displaying only negative  $R^Q$  values for one explanatory case (S19), is presented in Fig. 8, where also  $Q(t)$  at STJ is displayed together with a probed  $V_{ax}(t)$  waveform: overall,  $Q(t)$  vs.  $V_{ax}(t)$  negative correlation values identify opposite flow direction between the driving flow rate and local axial fluid velocity inside the aorta. Such regions of negative correlation are located at the AAO inner wall (Fig. 8), consistent with visualizations in Fig. 4.

The anatomical length of persistence of the correlation between  $Q(t)$  at STJ and  $V_{ax}(t)$  waveforms within individual healthy aortas as given by the  $AWCD$  metric (median value 0.296, IQR 0.231–0.339) is visualized in Fig. 7(B). Consistent with  $R^Q$  distributions, individual aortas characterized by an overall very high dynamical similarity between  $Q(t)$  waveform at STJ and distal  $V_{ax}(t)$  waveforms exhibit high  $AWCD$  values: in those aortas the dynamic similarity of large-scale advective blood flow with the driving flow rate at STJ persists up to the aortic arch and extends to cover between the 33% to 40% of the thoracic aorta length (Fig. 7(B)). For those individual aortas where  $R^Q$  values are overall smaller than the threshold value  $\hat{R}^Q$ , the  $Q(t)$ - $V_{ax}(t)$  dynamic similarity vanishes in the proximal AAO within a distance from the STJ between 13% and 22% of the thoracic aorta length (Fig. 7(B)). In intermediate cases (e.g., subjects S4, S5, S7, S9, S14) the dynamic similarity is preserved up to the distal end of the AAO, on average.

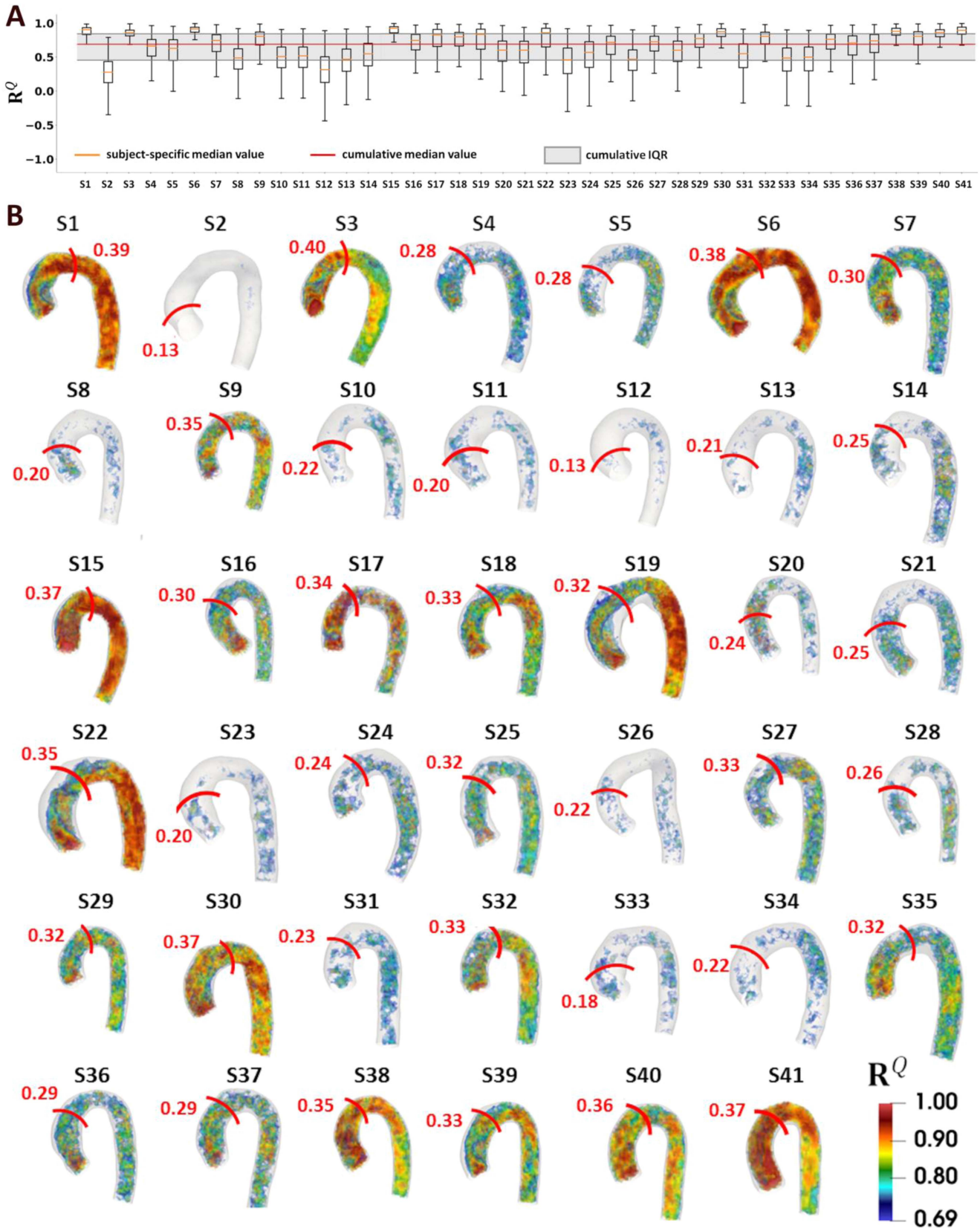


Fig. 7. (A) Box plots and (B) volumetric maps of correlation coefficients  $R^Q$  between the blood flow rate waveform  $Q(t)$  at STJ and axial velocity waveforms  $V_{a,x}(t)$  in the “one-to-all” networks. Volumetric maps show only  $R^Q$  values above the cumulative median value ( $\hat{R}^Q = 0.69$ ). In panel (B), the average weighted curvilinear distance (AWCD) is indicated on each aorta with a red line. Reconstructed geometries are shown with different scales. IQR: interquartile range.

TABLE II  
 $AWCD$  DISTRIBUTION IN LOW, MEDIUM, AND HIGH  $\bar{Q}$  AND  $Q_{p-p}$  TERTILE GROUPS

	$\bar{Q}$			$Q_{p-p}$		
	Low	Medium	High	Low	Medium	High
$AWCD$	0.223 (0.203-0.261)	0.286 (0.240-0.353)	0.336 (0.325-0.369)	0.243 (0.208-0.319)	0.294 (0.239-0.342)	0.325 (0.283-0.369)

For each tertile group,  $AWCD$  is expressed as median (interquartile range, IQR).

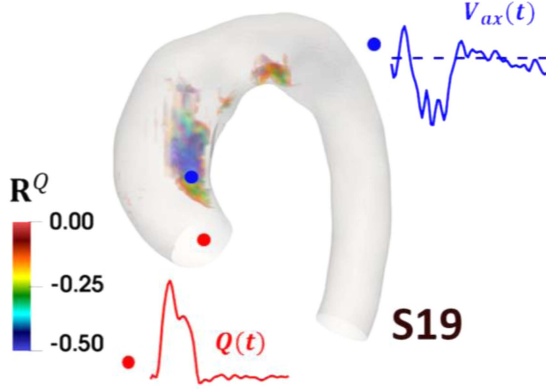


Fig. 8. Explanatory example of negative correlations  $R^Q$  between the blood flow rate waveform  $Q(t)$  at STJ and axial velocity waveforms  $V_{ax}(t)$  in one representative case. Negative correlations mainly characterize the regions of flow reversal at the inner AAO, where  $V_{ax}(t)$  waveforms exhibit negative values. Waveforms shown in the figure were interpolated for visualization purposes.

### E. Association of the Correlation Persistence Length With Geometric Attributes and Blood Flow Rate Waveform Features

No association between the persistence length of the correlation of  $Q(t)$  waveform at STJ with  $V_{ax}(t)$  waveforms as measured by  $AWCD$  and the geometric attributes of the aorta emerged. Similarly, no association emerged between  $AWCD$  and aortic stiffness.

The anatomical length of persistence of the correlation within the healthy aorta was found to be associated with the cycle-averaged value  $\bar{Q}$  and peak-to-peak amplitude  $Q_{p-p}$  of the blood flow rate waveform at STJ. In detail,  $AWCD$  was positively correlated with  $\bar{Q}$  ( $R = 0.65$ ,  $p < 0.0001$ , Fig. 9), suggesting that higher average blood flow rate values promote the propagation of large-scale fluid structures similarity for longer distances inside the aorta. When dividing the  $AWCD$  distribution into three groups based on the tertile values of the ranked  $\bar{Q}$  data (Table II), significant differences in  $AWCD$  emerged among all the three  $\bar{Q}$  groups ( $p < 0.001$ ), as well as between low and intermediate ( $p = 0.02$ ), low and high ( $p < 0.0001$ ), and intermediate and high ( $p = 0.04$ ) tertile groups (Fig. 9). Moreover,  $AWCD$  was found to be correlated with  $Q_{p-p}$  ( $R = 0.36$ ,  $p = 0.02$ , Fig. 9). Significant differences ( $p = 0.03$ , Fig. 9) in  $AWCD$  values emerged between  $Q_{p-p}$  low and high tertile groups (Table II), suggesting that a strong fluctuation of the blood flow rate waveform at STJ promotes the propagation of correlation between the driving  $Q(t)$  waveform at STJ and the axial velocities within the distal aorta. No association emerged between  $AWCD$  and  $Q_{PI}$ .

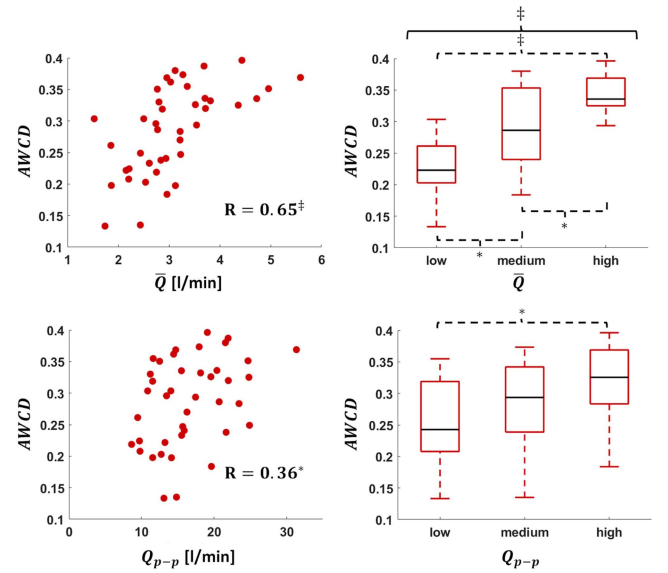


Fig. 9. Scatter plot of blood flow rate cycle-average value  $\bar{Q}$  or peak-to-peak amplitude  $Q_{p-p}$  vs. average weighted curvilinear distance  $AWCD$  (left panel). Box plots comparing  $AWCD$  distributions obtained by dividing  $\bar{Q}$  and  $Q_{p-p}$  in three groups based on the respective tertile values (right panel).  $R$ : Spearman correlation coefficient. Statistical significance is indicated with: \* $p < 0.05$ ; † $p < 0.01$ ; ‡ $p < 0.001$ .

## IV. DISCUSSION

Aortic hemodynamics is an intricate four-dimensional process involving non-trivial interactions and re-organization of fluid structures at all the scales of motion [7], [8], [11], [13], [38], [39]. A large body of literature evidences the effort expended to decipher the complexities of aortic hemodynamics, aiming at extracting information of physiological and/or pathological significance [6], [9], [20], [22], [40]. The richness of spatiotemporal information made available by personalized in silico and in vitro models of the aortic hemodynamics as well as by non-invasive imaging techniques such as 4D flow MRI has been methodologically faced adopting a reductionist approach. The choice for a reductionist approach was dictated by the need of distilling the hemodynamic complexity into threshold values of quantities to be used for diagnostic and prognostic purposes, and ultimately for clinical decision-making. The practical fallout of such reductionism was that clinically-oriented characterizations of aortic hemodynamics focused mainly on (surface-, volume- and time-) averaged fluid-related quantities or on a single instantaneous snapshot, potentially hindering a wider exploration of blood flow and ultimately overlooking important flow field organization features that (1) are hidden in the complex nature

of aortic hemodynamics and (2) can be retained or disrupted due to geometric attributes and/or in presence of developing pathologies of the aorta.

Aiming at recovering part of the information lost, here we adopted a recently-proposed method based on complex networks theory, where cardiovascular flows are assimilated to social networks [13], [28], [29], [30]. In detail, 4D flow MRI measurements of the human healthy aorta hemodynamics were integrated with a “one-to-all” network approach [28] to evaluate the role of blood flow rate waveform at STJ and aortic geometric attributes in the transport of flow coherence in the distal aorta, an aspect poorly investigated thus far.

Assuming blood flow rate at STJ and flow velocity waveforms in the aortic domain as individual units in a social network, with the correlations between  $Q(t)$  and  $V_{ax}(t)$  dynamic behaviors quantifying the similarity between “social” units, the here adopted networks paradigm allowed us a robust, quantitative definition of coherent large-scale aortic fluid structures [41]. The definition of flow coherence, still elusive and open to different interpretations, is here strengthened by (1) considering the flow rate waveform at the AAO as one of the driving factors conditioning aortic hemodynamics in healthy subjects, and (2) the computation of the persistence length of the correlation as given by the *AWCD* metric, which strategically emphasizes the correlations at those voxels located at longer distance from the STJ. In a previous study, we adopted a CNSs-based definition of flow coherence in a broader sense, analyzing the heterogeneity of the local hemodynamics in dilated and non-dilated aortas [13]. Here we focused on the coherence of large-scale aortic motion as imparted by the proximal AAO flow rate waveform. The choice of characterizing large-scale aortic motion using axial velocity, which represents the main flow direction, was supported by our recent findings highlighting that  $V_{ax}$  better captures the inter-variability of large-scale aortic flows, compared to the secondary (in-plane) flow structures, which appear more spatiotemporally homogeneous [13].

Among the main findings of the study, we report that in the healthy human aorta the anatomical persistence length of the correlation between the driving blood flow rate waveform at STJ and the distal motion in the main flow direction: (1) is characterized by an *AWCD* (median) value of 0.296 (IQR 0.231–0.339); (2) is positively associated with the cycle-averaged value of the blood flow rate as well as with its peak-to-peak amplitude; (3) is not associated with the main aortic geometric attributes nor with aortic stiffness.

Such findings are indicative of a remarkable inertial effect of blood flow rate at STJ on the spatiotemporal coherence of the distal aortic flow. Higher average blood flow rate values  $\bar{Q}$  in the proximal AAO have marked impact on aortic flow inertia, with the consequence of transporting the dynamic similarity between  $Q(t)$  and large-scale fluid structures more distally, thus covering longer aortic segments downstream of the STJ. A further contribution to transport hemodynamic similarity is given by high  $Q_{p-p}$  values, i.e. large peak-to-peak amplitude blood flow rate waveforms at proximal AAO feed correlation propagation, even if to a lesser extent compared to  $\bar{Q}$ . Consistent with the present results, a previous *in vivo* study [42] based on

4D flow MRI acquisitions on ostensibly healthy aortas indicated that the stroke volume normalized by the aortic volume, i.e., a quantity directly linked to  $\bar{Q}$ , plays a greater role than aortic curvature, arch shape, ascending aortic angle or diameter in shaping aortic flow features in terms of flow velocity, vorticity and helicity but only in subjects older than 33 years of age. Consistently, in this study, where 24 out of the 41 investigated subjects are above 33 years of age, cycle-average blood flow rate  $\bar{Q}$  but not curvature significantly influences the distal transport of large-scale fluid structures.

The main results of this study may be overturned in the presence of pathological conditions characterized by macroscopic morphological alterations of the aorta (aneurysm, dissection, coarctation) [9], [16], [22], [23], [43], in presence of pathological or abnormal aortic valves or implantable devices (prosthetic aortic valves, endografts), or in case of abnormal tortuosity. All those cases have been associated with the presence of flow disturbances in the aorta [23], [30], [43], [44], [45]. Such geometrical abnormalities are expected to influence the organization of large-scale coherent fluid structures at different levels, depending e.g., on the severity of the pathology. In this regard, several previous *in vivo* studies [9], [11], [23], [46] demonstrated that the incidence of alterations in aortic blood flow patterns is significantly increased in patients with dilated AAO and leads to disease progression [18], [19]. In this respect, a recent study integrating complex networks theory with computational hemodynamics suggested that the anatomical length of correlation persistence of axial flow patterns in aorta is shortened in the presence of AAO dilation [30]. Moreover, this effect on the anatomical length of correlation persistence is linked to the AAO dilation level, as demonstrated *in vivo* on dilated and non-dilated AAO [13].

The present approach may also prove useful to provide a quantitative indication of the restoration of normal blood flow features and recovered flow organization in the DAAo, i.e., distal to the hemodynamic or morphological pathological alteration [11], [47]. In this context, the findings of this “one-to-all” analysis contribute to non-invasively identify and measure distinguishable physiological, coherent large-scale hemodynamic features of the healthy human aorta, which may serve as reference for future studies involving large dataset of diseased aortas, ultimately improving the understanding of the impact of: (1) morphological alterations caused by aortic diseases on hemodynamic coherence loss; (2) specific surgical interventions or devices implantation in restoring/disrupting the physiological spatiotemporal correlation in large-scale aortic flows.

This study has some limitations. The correlations between aortic blood flow rate waveform at STJ and distal large-scale motion in the “one-to-all” analysis may be affected by noise. However, correlations are expected to be driven by the systolic phase, which is characterized by a higher signal-to-noise ratio compared to the diastolic phase, therefore dampening the effect of noise on the correlations [13]. In addition to that, since all 4D flow MRI acquisitions were made using the same protocol and analyzed with the same methods, inter-subject comparisons were unbiased. Moreover, here we tested a limited number of geometric parameters to describe aortic morphology. Further

descriptors should be considered for a more comprehensive description of the complex aortic 3D geometry. Another limitation is the relatively small sample size ( $n = 41$ ) considered in this study. Therefore, further investigations with larger datasets are needed to confirm the present findings.

## V. CONCLUSION

In this study, a quantitative in vivo characterization of the large-scale coherent blood flow motion in the healthy human aorta with 4D Flow MRI is proposed. Assimilating the aortic flow to a social network, a “one-to-all” network strategy is adopted to quantitatively assess non-invasively the similarity of blood flow patterns in the aorta with proximal aortic flow rate waveform, here assumed as a main factor conditioning the aortic hemodynamics. To elucidate the flow physics underlying the anatomical length of persistence of such similarity, the impact of blood flow rate waveform in the proximal ascending aorta and of the main aortic geometric attributes was investigated. Our findings suggest that (higher) average and peak-to-peak blood flow rate values in the healthy ascending aorta dictate the (longer) propagation of flow coherence of large-scale blood structures in the distal aorta, because of the imparted fluid inertia. Conversely, neither the anatomy nor the stiffness of the healthy aorta play a major role in this phenomenon.

In the future, by extending the analysis to diseased aortas, the flow features emerged from the “one-to-all” network-based study on healthy aortas may be used as reference values for diagnostic and predictive purposes, facilitating the comprehension of those flow-mediated mechanisms behind the pathogenesis of aortic disease, and finally providing a reference framework of physiological significance to be adopted also for the design and performance optimization of implantable devices.

## REFERENCES

- [1] T. L. Yearwood and K. B. Chandran, “Physiological pulsatile flow experiments in a model of the human aortic arch,” *J. Biomech.*, vol. 15, no. 9, pp. 683–704, Jan. 1982.
- [2] K. B. Chandran, “Flow dynamics in the human aorta,” *J. Biomechanical Eng.*, vol. 115, no. 4B, pp. 611–616, Nov. 1993.
- [3] B. J. Bellhouse and L. Talbot, “The fluid mechanics of the aortic valve,” *J. Fluid Mechanics*, vol. 35, no. 4, pp. 721–735, 1969.
- [4] P. P. Sengupta et al., “Twist mechanics of the left ventricle: Principles and application,” *JACC Cardiovasc. Imag.*, vol. 1, no. 3, pp. 366–376, 2008.
- [5] U. Morbiducci et al., “In vivo quantification of helical blood flow in human aorta by time-resolved three-dimensional cine phase contrast magnetic resonance imaging,” *Ann. Biomed. Eng.*, vol. 37, no. 3, pp. 516–531, Mar. 2009.
- [6] A. Frydrychowicz et al., “Time-resolved magnetic resonance angiography and flow-sensitive 4-dimensional magnetic resonance imaging at 3 Tesla for blood flow and wall shear stress analysis,” *J. Thoracic Cardiovasc. Surg.*, vol. 136, no. 2, pp. 400–407, Aug. 2008.
- [7] A. Frydrychowicz et al., “Interdependencies of aortic arch secondary flow patterns, geometry, and age analysed by 4-dimensional phase contrast magnetic resonance imaging at 3 Tesla,” *Eur. Radiol.*, vol. 22, no. 5, pp. 1122–1130, May 2012.
- [8] U. Morbiducci et al., “Mechanistic insight into the physiological relevance of helical blood flow in the human aorta: An in vivo study,” *Biomech. Model. Mechanobiology*, vol. 10, no. 3, pp. 339–355, Jun. 2011.
- [9] J. Burk et al., “Evaluation of 3D blood flow patterns and wall shear stress in the normal and dilated thoracic aorta using flow-sensitive 4D CMR,” *J. Cardiovasc. Magn. Reson.*, vol. 14, Dec. 2012, Art. no. 84.
- [10] P. J. Kilner et al., “Helical and retrograde secondary flow patterns in the aortic arch studied by three-directional magnetic resonance velocity mapping,” *Circulation*, vol. 88, no. 5, pp. 2235–2247, Nov. 1993.
- [11] M. Markl et al., “Time-resolved 3-dimensional velocity mapping in the thoracic aorta: Visualization of 3-directional blood flow patterns in healthy volunteers and patients,” *J. Comput. Assist. Tomography*, vol. 28, no. 4, pp. 459–468, 2004.
- [12] M. Markl et al., “Comprehensive 4D velocity mapping of the heart and great vessels by cardiovascular magnetic resonance,” *J. Cardiovasc. Magn. Reson.*, vol. 13, no. 1, pp. 1–22, 2011.
- [13] K. Calò et al., “Combining 4D flow MRI and complex networks theory to characterize the hemodynamic heterogeneity in dilated and Non-dilated human ascending aortas,” *Ann. Biomed. Eng.*, vol. 49, no. 9, pp. 2441–2453, 2021.
- [14] X. Shen et al., “Voxel-by-voxel 4D flow MRI-based assessment of regional reverse flow in the aorta,” *J. Magn. Reson. Imag.*, vol. 47, no. 5, pp. 1276–1286, 2018.
- [15] D. G. Guzzardi et al., “Valve-related hemodynamics mediate human bicuspid aortopathy: Insights from wall shear stress mapping,” *J. Amer. College Cardiol.*, vol. 66, no. 8, pp. 892–900, Aug. 2015.
- [16] P. van Ooij et al., “Fully quantitative mapping of abnormal aortic velocity and wall shear stress direction in patients with bicuspid aortic valves and repaired coarctation using 4D flow cardiovascular magnetic resonance,” *J. Cardiovasc. Magn. Reson. Official J. Soc. Cardiovasc. Magn. Reson.*, vol. 23, no. 1, Feb. 2021, Art. no. 9.
- [17] M. M. Bissell et al., “Aortic dilation in bicuspid aortic valve disease: Flow pattern is a major contributor and differs with valve fusion type,” *Circulation: Cardiovasc. Imag.*, vol. 6, no. 4, pp. 499–507, 2013.
- [18] S. C. S. Minderhoud et al., “Wall shear stress angle determines aortic growth in patients with bicuspid aortic valves,” *Eur. Heart J.: Cardiovasc. Imag.*, vol. 22, 2021, Art. no. jeab090-120.
- [19] A. Guala et al., “Wall shear stress predicts aortic dilation in patients with bicuspid aortic valve,” *Cardiovasc. Imag.*, vol. 15, no. 1, pp. 46–56, 2022.
- [20] M. D. Hope et al., “Bicuspid aortic valve: Four-dimensional MR evaluation of ascending aortic systolic flow patterns,” *Radiology*, vol. 255, no. 1, pp. 53–61, Apr. 2010.
- [21] A. F. Hassanabad et al., “Pressure drop mapping using 4D flow MRI in patients with bicuspid aortic valve disease: A novel marker of valvular obstruction,” *Magn. Reson. Imag.*, vol. 65, pp. 175–182, Jan. 2020.
- [22] L. Dux-Santoy et al., “Increased rotational flow in the proximal aortic arch is associated with its dilation in bicuspid aortic valve disease,” *Eur. Heart J.: Cardiovasc. Imag.*, vol. 20, no. 12, pp. 1407–1417, Mar. 2019.
- [23] J. F. Rodríguez-Palomares et al., “Aortic flow patterns and wall shear stress maps by 4D-flow cardiovascular magnetic resonance in the assessment of aortic dilatation in bicuspid aortic valve disease,” *J. Cardiovasc. Magn. Reson.*, vol. 20, no. 1, 2018, Art. no. 28.
- [24] J. von Spiczak et al., “Quantitative analysis of vortical blood flow in the thoracic aorta using 4D phase contrast MRI,” *PLoS One*, vol. 10, no. 9, 2015, Art. no. e0139025.
- [25] M. Markl et al., “4D flow imaging: Current status to future clinical applications,” *Curr. Cardiol. Rep.*, vol. 16, no. 5, pp. 1–9, 2014.
- [26] S. C. Shadden and C. A. Taylor, “Characterization of coherent structures in the cardiovascular system,” *Annu. Rev. Biomed. Eng.*, vol. 36, no. 7, pp. 1152–1162, 2008.
- [27] M. Newman, *Networks*. Oxford, U.K.: Oxford Univ. Press, 2018.
- [28] K. Calò et al., “Spatiotemporal hemodynamic complexity in carotid arteries: An integrated computational hemodynamics and complex networks-based approach,” *IEEE Trans. Biomed. Eng.*, vol. 67, no. 7, pp. 1841–1853, Jul. 2020.
- [29] K. Calò et al., “Exploring wall shear stress spatiotemporal heterogeneity in coronary arteries combining correlation-based analysis and complex networks with computational hemodynamics,” *Proc. Inst. Mech. Engineers Part H: J. Eng. Med.*, vol. 234, no. 11, pp. 1209–1222, 2020.
- [30] G. De Nisco et al., “Deciphering ascending thoracic aortic aneurysm hemodynamics in relation to biomechanical properties,” *Med. Eng. Phys.*, vol. 82, pp. 119–129, Aug. 2020.
- [31] U. Morbiducci et al., “A rational approach to defining principal axes of multidirectional wall shear stress in realistic vascular geometries, with application to the study of the influence of helical flow on wall shear stress directionality in aorta,” *J. Biomech.*, vol. 48, no. 6, pp. 899–906, Apr. 2015.
- [32] K. M. Johnson et al., “Improved 3D phase contrast MRI with off-resonance corrected dual echo VIPR,” *Magn. Reson. Med.*, vol. 60, no. 6, pp. 1329–1336, Dec. 2008.

- [33] M. H. Friedman et al., "Arterial geometry affects hemodynamics: A potential risk factor for atherosclerosis," *Atherosclerosis*, vol. 46, no. 2, pp. 225–231, 1983.
- [34] D. Gallo et al., "An insight into the mechanistic role of the common carotid artery on the hemodynamics at the carotid bifurcation," *Ann. Biomed. Eng.*, vol. 43, no. 1, pp. 68–81, Jan. 2015.
- [35] P. Ou et al., "Late systemic hypertension and aortic arch geometry after successful repair of coarctation of the aorta," *Eur. Heart J.*, vol. 25, no. 20, pp. 1853–1859, 2004.
- [36] I. Bargiotas et al., "Estimation of aortic pulse wave transit time in cardiovascular magnetic resonance using complex wavelet cross-spectrum analysis," *J. Cardiovasc. Magn. Reson. Official J. Soc. Cardiovasc. Magn. Reson.*, vol. 17, no. 1, Jul. 2015, Art. no. 65.
- [37] A. Guala et al., "Influence of aortic dilation on the regional aortic stiffness of bicuspid aortic valve assessed by 4-dimensional flow cardiac magnetic resonance: Comparison with marfan syndrome and degenerative aortic aneurysm," *JACC Cardiovasc. Imag.*, vol. 12, no. 6, pp. 1020–1029, Jun. 2019.
- [38] H. G. Bogren and M. H. Buonocore, "4D magnetic resonance velocity mapping of blood flow patterns in the aorta in young vs. elderly normal subjects," *J. Magn. Reson. Imag.*, vol. 10, no. 5, pp. 861–869, Nov. 1999.
- [39] M. Sigovan et al., "Comparison of four-dimensional flow parameters for quantification of flow eccentricity in the ascending aorta," *J. Magn. Reson. Imag.*, vol. 34, no. 5, pp. 1226–1230, Nov. 2011.
- [40] S. Pirola et al., "4-D flow MRI-based computational analysis of blood flow in patient-specific aortic dissection," *IEEE Trans. Biomed. Eng.*, vol. 66, no. 12, pp. 3411–3419, Dec. 2019.
- [41] S. K. Robinson, "Coherent motions in the turbulent boundary layer," *Annu. Rev. Fluid Mechanics*, vol. 23, no. 1, pp. 601–639, 1991.
- [42] F. M. Callaghan et al., "Age-related changes of shape and flow dynamics in healthy adult aortas: A 4D flow MRI study," *J. Magn. Reson. Imag.*, vol. 49, no. 1, pp. 90–100, 2019.
- [43] M. Salmasi et al., "In-vivo blood flow parameters can predict at-risk aortic aneurysms and dissection: A comprehensive biomechanics model," *Eur. Heart J.*, vol. 41, no. Supplement\_2, 2020, Art. no. ehaa946-2339.
- [44] O. A. Jarral et al., "Phase-contrast magnetic resonance imaging and computational fluid dynamics assessment of thoracic aorta blood flow: A literature review," *Eur. Assoc. Cardio-Thoracic Surg. Official J. Eur. Assoc. Cardio-Thoracic Surg.*, vol. 57, no. 3, pp. 438–446, Mar. 2020.
- [45] F. Condemni et al., "Ascending thoracic aorta aneurysm repair induces positive hemodynamic outcomes in a patient with unchanged bicuspid aortic valve," *J. Biomech.*, vol. 81, pp. 145–148, Nov. 2018.
- [46] E. T. Biegging et al., "In vivo three-dimensional MR wall shear stress estimation in ascending aortic dilatation," *J. Magn. Reson. Imag.*, vol. 33, no. 3, pp. 589–597, Mar. 2011.
- [47] A. Frydrychowicz et al., "Time-resolved, 3-dimensional magnetic resonance flow analysis at 3 T: Visualization of normal and pathological aortic vascular hemodynamics," *J. Comput. Assist. Tomography*, vol. 31, no. 1, pp. 9–15, 2007.

Open Access provided by 'Politecnico di Torino' within the CRUI CARE Agreement